Check for updates

An unusual mixed-valence cobalt dimer as a catalyst for the anti-Markovnikov hydrophosphination of alkynes†

Pardeep Kumar, Asmita Sen, Gopalan Rajaraman (ID) * and
Maheswaran Shanmugam (ID) *

The reaction of $[Co(PMe_3)_4]$ (**1**) with a redox-active NNN pincer ligand (L_1) led us to isolate a unique binuclear cobalt complex ($[(PMe_3)_2Co^{II}(L_1^{3-})Co^I(PMe_3)_3]$ (**2**)) anchored by a three-electron reduced L_1 in its unusual coordination mode. Such an unprecedented binuclear pincer/allyl cobalt complex consisting of the mixed-valence oxidation state of cobalt ions (+1 and +2) is confirmed by various analytical techniques (XPS, EPR, and UV–vis), and the experimentally determined electronic structure is well corroborated by detailed theoretical studies based on DFT calculations. Complex **2** efficiently catalyzes the hydrophosphination of alkynes regioselectively, and affords the anti-Markovnikov product in good to excellent yields without any additional strong bases or organolithium reagents. Both internal and terminal alkynes including propargylic alcohols were amenabled to accessing vinyl trivalent phosphines with exclusive E-selectivity. The isotopic labeling experiments confirmed the 1,2-anti-Markovnikov addition of P–H from $HPPh_2$ across the alkyne stem. The preliminary ^1H and ^{31}P NMR investigations revealed that the Co^I nucleus in **2** is likely responsible for the catalytic outcome of the hydrophosphination of alkynes. Overall, the study discloses the importance of the exemplary structural platform offered by the redox-active pincer ligands in isolating unusual multi-nuclear complexes and the need to explore the multi-nuclear complexes as a catalyst besides the traditional mononuclear catalyst.

Introduction

The exciting electronic structure and the physicochemical and catalytic properties exerted by redox-active pincer ligands (such as L_1) with alkali, transition or main group metal ions are very interesting and an active area of research.[1–8] The reduction of NNN-type pincer ligands by more than two electrons is an extremely challenging task, as evidenced by the limited number of such complexes reported to date.[9–13] Developing a synthetic strategy and stabilising such magnificent molecules are of wide interest for activating small, thermodynamically stable molecules such as H_2, N_2, CO_2, *etc.*, to utilise them as commodity chemicals, as well as other targeted catalytic

Department of Chemistry, Indian Institute of Technology Bombay, Powai, Mumbai-400076, Maharashtra, India. E-mail: eswar@chem.iitb.ac.in, rajaraman@chem.iitb.ac.in

activities.[14,15] Although several synthetic routes are available to isolate three-electron reduced-NNN pincer ligand complexes, the synthetic method reported in this article is distinct from the reported methods.[9–11,16]

Despite the redox-active metal complexes being used for various other catalytic activities,[17–25] the field is still in its infancy regarding the hydro-functionalisation (such as hydrosilylation, hydroboration, hydroamination, hydrothiolation, and hydrophosphination, *etc.*) of C–X (where X = O, N, S or C) unsaturated bonds. The addition of an X–H (X = a heteroatom such as P, N, or S) group across C–C multiple bonds possesses significant importance due to its atom economy and step economy as it does not produce any waste/side products. Among the various hydro-functionalisation reactions, the hydrophosphination reaction is considered as an important catalytic reaction, as the organophosphorus compounds can be used as potential ligands in metal catalysis, as antibiotics, and as anti-tumor agents.[26–28] However, the development of catalysts for hydrophosphination/hydrothiolation reactions is extremely sluggish due to the poisoning of the metal catalyst by the reaction products.[29–31] Noble metals such as [Pt], [Pd], and [Ru], and other metal catalysts, have been explored for the hydrophosphination of activated alkene/alkynes,[32–34] while the

3d transition metals are relatively less explored, partly due to catalyst poisoning or poor selectivity, and require strong bases such as n-BuLi to achieve the vinyl phosphines.[34–36] Among the various 3d metal ion catalysts unveiled, only a limited number of catalysts are capable of adding P–H across alkynes for both terminal and internal alkynes.[37–41] However, the functional group at the propargylic position is seldom explored. This demands an alternative strategy for the catalyst design, and in particular, the employed ligand must anchor the metal ion with a less vacant site for coordination to avoid catalyst poisoning by the products arising from the reaction. Herein we unveil a novel, redox-active cobalt complex anchored on a NNN pincer ligand[11] with the molecular formula $[(PMe_3)_2Co^{II}(L_1^{3-})Co^{I}(PMe_3)_3]$ (**2**). **2** was found to be an efficient catalyst for the hydrophosphination of terminal (including α-functionalized alkynes) and internal alkynes, where the P–H bond adds to the alkyne to provide anti-Markovnikov addition products. The catalytic efficiency of **2** exceeds that of certain mononuclear 3d metal ion catalysts and certainly shows an improved turnover number compared with the other dinuclear catalysts reported in the literature (*vide infra*). The cobalt ion that actively participates in the catalytic cycle was disclosed based on detailed ^{1}H and ^{31}P NMR experiments. In addition, the detailed electronic structure of **2** was investigated using various analytical techniques (XPS, UV–vis, and EPR) and corroborated by theoretical calculations.

Experimental

Methods and material

Unless otherwise mentioned, all the reactions were performed under anaerobic conditions (Ar-atm.). All the alkyne substrates and solvents were purchased from commercially available sources (Sigma Aldrich and Alfa Aesar). $[Co(PMe_3)_4]$ was synthesized as per the literature method.[42] The EPR spectrum was produced at RT as well as 77 K under an Ar atmosphere on a JEOL instrument (JES-FA200 ESR spectrometer). The purity of the ligand and the catalysis reaction products was analyzed using Bruker 400 and 500 NMR instruments. The X-ray photoelectron spectrum of **2** was measured on a Kratos analytical electron spectrometer. The samples were mounted on carbon tape such that the sample cylinder was completely covered. The single-crystal X-ray data were collected on a Rigaku Saturn diffractometer using a graphite monochromator (MoKα, $\lambda = 0.71073$ Å). The CCDC numbers are 2062557 (for **2**), 2062558–2062563 and 2060385.†

Synthesis of NNN-pincer ligand (2,6-bis(2-iminomesityl-benzyl)pyridine) (L_1).
To the 100 mL, two-neck RB flask containing a toluene solution (50 mL) of 2,6-dibenzoyl pyridine (2.0 g, 6.96 mmol), p-toluene sulfonic acid (198 mg, 15 mol%) was added. This reaction mixture was stirred at room temperature for 30 minutes before 2,4,6-trimethyl aniline (2.12 g, 15.7 mmol) was added, which was heated under reflux for 48 hours. (Note: Releasing the generated pressure during reflux is mandatory. Also, the condensed water was collected using the Dean–Stark apparatus.) After the completion of the reaction, the solvent was removed using a rotovap. This resulted in an oily mass that was dissolved in 20% ethyl acetate in petroleum ether (30 mL). The solution was passed through a neutral alumina and Na_2SO_4 mixture. The collected filtrate was concentrated and kept for crystallization at −20 °C. Block-shaped yellow crystals were grown from the filtrate overnight. Yield = 2.0 g (55%).

Synthesis of $[(PMe_3)_2Co^{II}(L_1^{3-})Co^{I}(PMe_3)_3]$, 2. L_1 (100 mg, 0.192 mmol) was dissolved in dry THF. To this yellow solution, two equivalents of **1** (139.25 mg, 0.383 mmol) were added. As a consequence, the yellow solution changed in color from yellow to dark brown immediately. This reaction mixture was stirred for 24 hours. After this, the solvent was removed under reduced pressure, resulting in a brown crude mass. The product of interest was extracted from the mass using hexane. The filtrate was filtered (G4 frit) and kept for crystallization at −25 °C. The brown single crystals of X-ray quality were grown from the filtrate within 24 hours (Scheme 1). Yield: 108 mg (55%).

The experimental procedure followed for the catalytic (hydrophosphination) reaction. In an argon-filled glove box, an airtight reaction tube was charged with 12 mg of **2** (2 mol%) and 2 ml dried toluene was added to it. 100 μl (107 mg, 0.57 mmol) of diphenylphosphine (HPPh₂) was added to the above mixture along with the corresponding alkyne substrate (0.57 mmol). The reaction tube was closed tightly and it was taken out of the glove box. The reaction mixture was heated at 60 °C for 1 hour. After completion of the reaction, the reaction vessel was cooled to room temperature, and instantly S_8 (20.24 mg, 0.63 mmol) was added. This was stirred for another 30 minutes. The reaction contents were passed through a bed of Celite. Then the collected filtrate was concentrated and passed through the silica column, which was eluted with the eluent (1% ethyl acetate in petroleum ether).

Computational methods

Unrestrained geometry optimization of **2** was carried out employing the density functional theory (DFT) method using the Gaussian 09 suite of programs.[43,44] The crystal structure of the catalyst was considered as the starting coordinates for the geometry optimizations, and Noodleman's broken symmetry (BS) approach[45] was employed to treat the Co^{II} centre and the radical centre. Herein we have treated the Co^{I} centre as d^8-low-
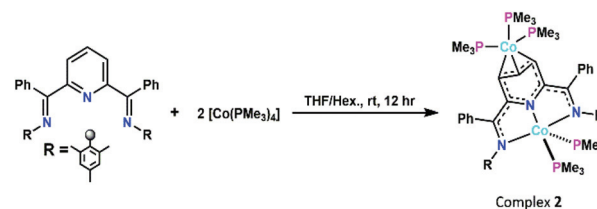
Scheme 1 The synthetic scheme followed to isolate **2**.

spin in accordance with the experimental observation, and therefore a total of four spin states were taken into account by varying the possible spin states of the Co^{II} centre – a high-spin, $S = 3/2$, and a low-spin, $S = 1/2$, spin states ferromagnetically and antiferromagnetically coupled with the radical. A dispersion-corrected unrestricted B3LYP-D3 hybrid density functional[46–51] has been employed. A TZV basis set is employed for both metal centres (Co^I and Co^{II}) and some of the atoms in the non-innocent NNN pincer ligand (L_1) which are directly involved in the charge and spin delocalisation, containing three NNN atoms (N1, N2 and N3), all carbons in the pyridinium ring of L_1 (C8–C12) and two carbons connecting the ring with N2 and N3 (C7 and C13). The rest of the atoms (P, C and H) were treated using the Ahlrichs split valence SVP basis set.[48,50]

All optimized geometries correspond to the global minima in their respective spin surfaces and are indicated by all of the positive frequencies from the harmonic vibrational frequency calculations on the optimized geometries at 298.15 K. The final quoted energies are the Gibbs free energy-corrected electronic energies. The natural bonding orbital (NBO)[52] and spin natural orbital (SNO) analyses implemented in the Gaussian 09 program were performed to find the bonding patterns, orbital occupancy, spin densities and Wiberg bond-indices values. The optimized geometries and spin densities were visualized using the Chemcraft version 1.6.[53]

Results and discussion

We began our investigation by treating one equivalent of the NNN pincer ligand (L_1) with two equivalents of $[Co(PMe_3)_4]$ (**1**) in THF, leading us to isolate a mixed-valence homo dinuclear cobalt complex as shown in Scheme 1. This unusual $[(PMe_3)_2Co^{II}(L_1{}^{3-})Co^I(PMe_3)_3]$ complex (**2**) was structurally confirmed through solid-structural analysis. Complex **2** crystallized in the monoclinic, $C2/c$ space group (Fig. 1; see Table S1 of ESI† for more details).

Fig. 1 shows the coordination sites of both the cobalt ions that were completed by the reduced NNN pincer ligand and trimethyl phosphine ligands. Assigning the electronic structure of a metal complex containing a redox non-innocent ligand is quite challenging. Careful analysis and comparison of the structural parameters of **2** with the reported NNN pincer redox-active ligand complexes (Scheme 2) showed that L_1 (in **2**) was reduced by three electrons.

This is unambiguously reflected in the bond lengths of $C_{im}–N_{im}$ (1.354(3) Å and 1.380(2) Å) and $C_{im}–C_{py}$ (1.414(4) Å and 1.389(5) Å), where C_{im} and N_{im} represent the carbon and nitrogen atoms of the imine bond in the reduced L_1 in **2** while C_{py} denotes the *o*-carbon of the reduced L_1 in **2**. Moreover, the pyridine ring of the reduced L_1 lost its aromaticity, which is again supported by the lack of alternative short and long bonds in the pyridine ring (see Scheme 2). Therefore, the pyridine ring lost its planarity as well (see Fig. 1A and 1B).

The isolation of metal complexes with a three-electron reduced redox-active ligand is extremely scarce in the litera-
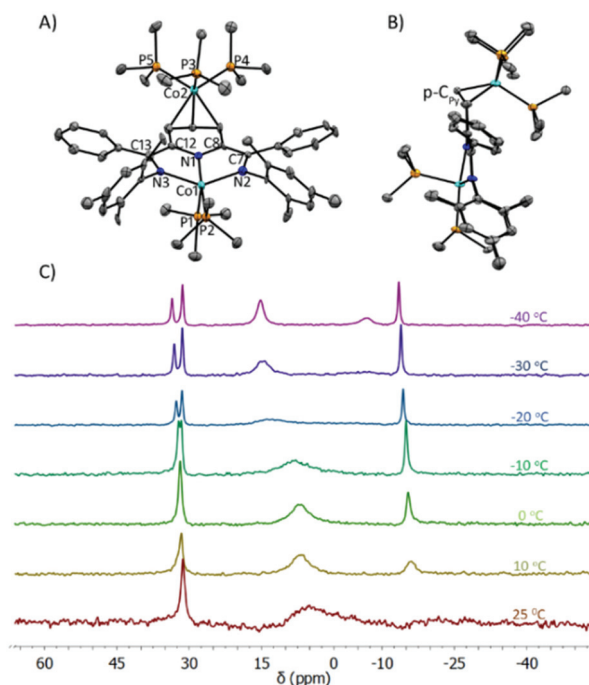

Fig. 1 (A) 50% probability of thermal ellipsoid representation of crystal structure of **2**. (B) An alternative view that shows the deformation observed in the pyridine ring of the reduced ligand in **2**. (C) The fluxional behaviour observed in **2** captured in variable-temperature ^{31}P-NMR spectra recorded in THF-d_8 solvent in 500 MHz instrument.
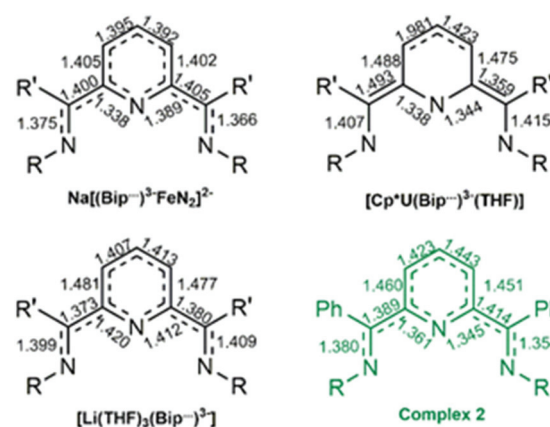
Scheme 2 The change in the bond lengths upon three-electron reduction of NNN pincer ligand[9–11] compared with the structural parameters observed for the ligand in **2**.

ture. Such complexes are often isolated by treating the neutral redox-active ligand and/or neutral complex with an excess of a reductant such as an alkali metal, NaH or metal alkyls (methyl lithium, trialkyl aluminum, or Grignard reagents). On the other hand, the distinct synthesis method followed here led us to isolate a unique binuclear cobalt complex (see Experimental details). The average deformation (Δd, which is nothing but the change in $C_{im}–N_{im}$ and $C_{im}–C_{Py}$ bond distances upon reduction of L_1 compared with its neutral ligand; Table S4 of

ESI†) calculated (0.09) from an empirical equation (eqn (1)) developed by Budzelaar and co-workers discloses further that the pincer ligand L$_1$ is reduced by more than two electrons (see Table S4 of ESI†).

$$\Gamma d = \frac{1}{2}[d_{C_{im}=N_{im}}(ave) - d^{0e}_{C_{im}=N_{im}}(ave) + d_{C_{im}-C_{py}}(ave) - d^{0e}_{C_{im}-C_{py}}(ave)]. \tag{1}$$

The absence of any counter anion in the crystal lattice of **2** and the reduction of L$_1$ by three electrons imply that the two cobalt centers should exist as a valence-localized mixed-valence system, *i.e.* one cobalt should be in the +2 and the other in the +1 oxidation state to neutralize the overall anionic charge of the reduced L$_1$. In **2**, the coordination modes are shown by L$_1{}^{3-}$ being quite distinct from other pincer ligands reported in the literature. The bond lengths observed for the cobalt ion (1.865–2.233 Å) occupying the NNN cavity of the reduced L$_1$ are much shorter than those of the cobalt ion (1.911–2.193 Å) anchored in the pyridine ring of the ligand ion **2**. Therefore, the cobalt ion (Co1) in the NNN cavity of **2** is assigned a 2+ oxidation state while the other one (Co2) is in a 1+ oxidation state. In general, phosphine ligands are strong σ-donor ligands; depending on the number of phosphine ligands, the metal complexes exist in either low-spin or high-spin states.

To establish the mixed-valence oxidation state of cobalt in **2**, we performed X-ray photoelectron spectroscopy (XPS) at room temperature (Fig. 2). In the XPS spectrum, the main photoelectron lines of cobalt 2p$_{3/2}$ and 2p$_{1/2}$ were observed at 777.6 eV and 793.76 eV respectively, along with the satellite peaks. Careful analysis of the primary photoelectron line's full width half maximum (FWHM) exceeds that of 3 eV, which is the normally expected FWHM for regular photoelectron lines. This implies that the binding energies (BE) of Co^I (BE = 777.40 eV) and Co^{II} (BE = 778.6 eV) fall into the same range, which can be deconvoluted by fitting the primary photoelectron lines. In general, determining the oxidation state of the metal ion only from the BE is often deceptive as the BE significantly changes depending upon the nature of the donor atoms co-

ordinated to it. For example, strong electron-donating atoms (such as phosphorous and nitrogen) coordinated to the metal ion will reduce the BE, while electron-withdrawing atoms (such as halides) will increase the BE of the metal ion.

However, the BE of the metal ions in **2** is significantly lower than those of the other Co^{II} or Co^I complexes reported in the literature. This is attributed to the strongly donating coordinating atoms (phosphorous and nitrogen) in **2**.[54,55] Further, careful analysis of the XPS spectrum shows that there is only one satellite peak observed. It is widely accepted and well exemplified in the literature already that the satellite peaks are observed only for the paramagnetic ions, not for diamagnetic metal ions. Therefore, Co^I is assigned as a diamagnetic low-spin ion (due to the presence of three phosphine ligands and a strong π-accepting allylic-type coordination environment, *vide infra*), while the Co^{II} ion is paramagnetic. The assignment of oxidation state is consistent with the other literature reports.[56–58]

To support the electronic structure determined for **2** using X-ray structure, XPS data and to determine the spin state of the paramagnetic Co^{II} ion, we have performed detailed theoretical calculations using density functional methods (see below). The Co1 in **2** exists in a distorted square pyramidal geometry where the three nitrogen donors of L$_1$ (Co–N$_{ave}$ = 1.93 ± 0.07 Å) and a PMe$_3$ (Co–P$_{eq.}$ = 2.229 Å) ligand occupy the equatorial plane while the apical site is occupied by the second PMe$_3$ ligand (Co–P$_{api.}$ = 2.233 Å). On the other hand, the Co2 in **2** shows an interesting and unique bonding mode, *i.e.* it is bound to the *meta* and *para* carbons of the pyridine ring (η^3) of the L$_1$ akin to the π-allyl ligand system. Such a coordination mode is extremely rare in the literature.[10,14,15,59,60] The remaining three coordination sites are occupied by three PMe$_3$ ligands. The selected bond distances and bond angles are provided in the ESI (see Tables S2 and S3).† The solid-state structure of **2** is maintained in the solution, which is evidently reflected in the variable-temperature ^{31}P NMR spectra of **2** (Fig. 1C and Fig. S20†). The presence of five different ^{31}P signals (30–35 ppm corresponds to the PMe$_3$ ligand in the Co1 center and +25 to −25 ppm is attributed to the PMe$_3$ ligand on the Co2 center) implies that all the PMe$_3$ ligands bound to the cobalt ions in **2** are in distinctly different environments, in addition to the fluxional behaviour observed.

Electronic structure and bonding of 2

DFT calculations using a hybrid B3LYP functional (see Computational details for more information) yield a spin-polarized $S = 0$ as the ground state for **2**, which arises due to the antiferromagnetic coupling between the Co^{II} in low spin ($S = 1/2$) and the resultant $S = 1/2$ spin originating from the three-electron reduced L$_1$. The corresponding ferromagnetic solution (triplet state; $S = 1$) is 12.7 kJ mol^{-1} higher in energy compared with the singlet ground state. If we assume that the Co^{II} centre has a high-spin $S = 3/2$ state, this will result in two pos-

Fig. 2 X-ray photoelectron spectrum of Co(2p) binding energy region in **2**.

sibilities: (i) an $S = 2$ state arising from a ferromagnetic coupling with the $S = 1/2$ spin present in the radical; and (ii) an $S = 1$ state due to antiferromagnetic interaction. The $S = 2$ state is higher in energy (27.0 kJ mol^{-1}) from the ground state, ruling out the possibility of involvement of this spin surface in the bonding/spectral features. The structural parameters of DFT optimized $S = 0$ ground spin state (both Co^{II} and Co^{I} ions) are in good agreement with the experimentally determined X-ray data (Tables S2 and S3 of ESI†). This offers confidence in our employed methodology, the determined ground state, and the electronic structure of the redox non-innocent complex of **2**.

Further, we performed spin natural orbital (SNO) analysis to elucidate the spin states as well as the electron distribution on both metal centres. The calculation reveals that, in the $S = 0$ ground state, the majority of the residual spin (0.86) remains in the d_{z^2} orbital of the Co^{II} centre, and the negative spin of the same amount is delocalized within the pyridinium Ns and the carbon and nitrogen atoms on the imine bond (Fig. S21†). A negligible amount of spin density is found on the Co^{I} centre, indicating that both metal centres are in a low-spin state and heavily spin polarised. The Co^{I} centre has hexa-coordination with three phosphine ligands, and the remaining coordination sites are satisfied by η^3-bonding to the allylic-like coordination mode formed by the *meta* and *para* carbons of the pyridine ring of the reduced L$_1$ ligand. The average Co^{I}–P bond distance is estimated to be 2.213 Å, while the average Co^{I}–η^3(C) bond is 2.061 Å. The bonds with the *meta*-carbons are longer (2.122 and 2.120 Å) than the bond with the *para*-position (1.942 Å) (Fig. 3). The geometry of the triplet excited state is not significantly different from the ground state structure (Table S5 of ESI†). The Co^{II}–N$_{ave}$ and Co^{II}–P$_{eq}$ bond distances are comparable with the ground state (1.965 and 2.311 Å), but the Co^{II}–P$_{api}$ bond is quite long (2.819 Å), indicating a pseudo Jahn–Teller distortion in this spin state.

Fig. 4 illustrates the frontier molecular orbitals of the singlet ground state ($S = ^1/_2$ spin on a Co^{II} centre antiferromagnetically coupled with a radical spin of $^1/_2$), where the SOMO of Co^{II} and the radical centre are shown. The splitting of the individual d-orbital indicates that the respective Co^{II} and Co^{I} centres are in the square pyramidal and octahedral geometries, although the α-/β-orbital degeneracy is lifted for the Co^{II} centre significantly due to the ligand environment as well as the Jahn Teller distortion. The Co^{II}-orbitals are deeply rooted, while the Co^{I}-orbitals are high lying and close to the singly occupied molecular orbital of the unpaired radical. Consequently, the HOMO–LUMO gap in Co^{II} is quite high (2.5 eV) as compared with that for Co^{I} (1.6 eV). The orbital splitting, as well as the HOMO–LUMO gap, indicates that Co^{I} reactivity is expected to be faster than that of Co^{II}. This is in good agreement with the experimental catalytic cycle presented in the following section (*vide infra*).

The DFT calculations have captured different bonding modes and charge distributions as well as spin delocalisation in reduced L$_1$. In the ground state, a spin-down β-electron is delocalised mainly on three pincer NNN donors (−0.168,

Fig. 3 B3LYP-D3 optimised geometry and spin density plot of (a) singlet ground state (Co^{II} low spin ($S = \frac{1}{2}$) antiferromagnetically coupled with radical spin $\frac{1}{2}$) and (b) close-lying triplet state (Co^{II} low spin ($S = \frac{1}{2}$) ferromagnetically coupled with radical spin $\frac{1}{2}$) of **2**.

Fig. 4 Frontier molecular orbitals of singlet ground state ($S = \frac{1}{2}$ antiferromagnetically coupled with radical spin $\frac{1}{2}$) showing the SOMO of Co^{II} and radical centre (energies are in eV).

−0.181, and −0.177 spins on N1–N3 respectively) and C7 (−0.198) and C13 (−0.170) carbon atoms while a negative charge is distributed in the Co^{I}-coordinated (η^3) π-allylic moiety (−0.725, −0.247, −0.856 charges on the C9–C11, respectively).

Similarly, in the high-lying triplet state, a spin-up α-electron is delocalised in a similar way (Table S5†). Therefore, the ligand L$_1$ is three-electrons reduced. The charge is delocalised among the *meta* and *para* carbons of the pyridine ring and the degeneracy is lifted, resulting in a η^3-coordination to Co2 (*i.e.* Co^I), while a more planar P2–N2–N1–N3 facilitates the unpaired spin being delocalized around the Co1 (*i.e.*, Co^{II}).

A higher partial double bond character (Wiberg bond index of 1.30, Table S5†) is found in C7–C8 and C12–C13 bonds, indicative of a more localised spin on these atoms, which is in line with the experimental observation. The η^3-bonding was also explored *via* the Natural Bonding Orbital (NBO) analysis. A 2c–2e bonding is found between the Co^I and C27 atoms of the allylic moiety involving the d$_{xy}$ orbital of Co (sd$^{2.53}$ hybridization) and the p$_z$ orbital of C27 (sp$^{13.71}$ hybridization). The other two Cs in the allylic group form a 2c–1e bond with the Co^I centre involving the d$_{yz}$ orbital of Co (sd$^{1.44}$ hybridization), the p$_x$ orbital of C34 (96.5% *p*-character), the d$_{yz}$ orbital of Co (sd$^{2.5}$ hybridization) and the p$_z$ orbital of C36 (93.2% *p*-character), respectively (Fig. S22†). As the ground singlet state and the first excited triplet states ($S = \frac{1}{2}$ in Co^{II} ferromagnetically coupled with the $S = \frac{1}{2}$ spin on the radical) are accessible and comparable with the thermal energy, we have computed the absorption spectra using TD-DFT for both low-lying spin states. The combination of these two states' absorption features (50% intensity of $S = 0$ and 50% intensity of $S = 1$) is comparable with the experimental UV–vis spectrum.

In the combined absorption spectra, a sharp peak at 336 nm is found, which is in excellent agreement with the experiment (342 nm). Broad features at 604 and 662 nm and a sharp feature at 448 nm are also in agreement with the experiments (486 and 528 nm, respectively; Fig. 5). All the transitions before 700 nm are due to metal to ligand or ligand to metal charge transfer, while a big hump around 954 nm, which is very weak in the experimentally determined spectra, is related to the triplet state and originates *via* d–d transition.
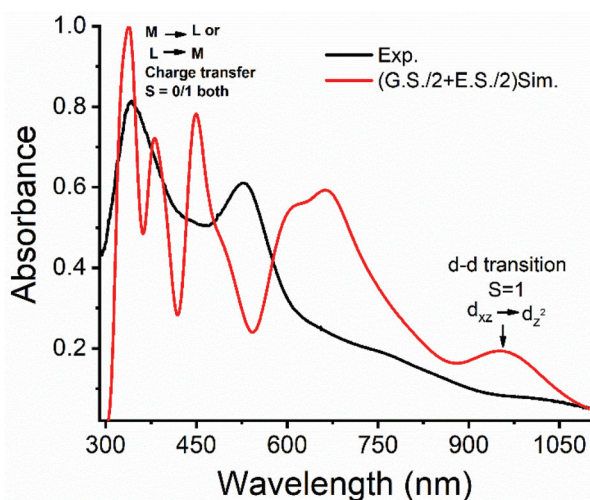
This broad-band is not captured in the TD-DFT spectra of the lowest-lying singlet ground state. Consistent with the theoretical observation and prediction, the X-band electron paramagnetic resonance (EPR) measurements performed on the powder sample of **2** were observed to be EPR active at room temperature, while the same being observed to be EPR silent at 77 K indicates that **2** possesses a singlet state as the ground state (Fig. S1 of ESI†). This EPR experiment further shows that the paramagnetic Co^{II} ion is in the low spin state. Based on the detailed experimental and theoretical calculations, we propose the electronic structure of **2** as in Scheme 3.

Having determined the correct electronic structure for this exotic molecule (**2**), we then focused on its catalytic application. In particular, the hydrophosphination of the alkynes as vinyl[61] phosphines was found to produce interesting ligands in catalysis.[62–66] The anti-Markovnikov *syn* addition of diphenylphosphine across the C–C triple bond (phenylacetylene) results in an *E*-vinylphosphine product (**3a**; Scheme 4). This air-stable product was isolated (after sulfidation) in nearly quantitative yield (89%), which gave an excellent TON compared with the other reported bimetallic catalysts used so far (Table S6 of ESI†). The anti-Markovnikov addition of P–H across the unsaturated bond was confirmed by isotopic labelling experiments where the hydrogen bound to the phosphine added to the internal carbon of the terminal alkyne (^{2}H NMR peak at 7.53 ppm; Fig. S2 of ESI†). The regio- and stereoselectivity predicted for these catalytic reactions was not only confirmed by NMR spectroscopy (^{1}H, ^{13}C, ^{31}P NMR spectra; see Fig. S3–S19 of ESI†), but also unambiguously by single-crystal X-ray diffraction for the majority of the products shown in Scheme 4. The single-crystal X-ray diffraction (see Table S7 of ESI†) of all the products shows that the aryl, alkyl or cyclic group of alkenes is *trans* to the –P=S group and the C–C double bond distance is observed to be 1.321 ± 0.022 Å in all the crystal structures of the products. To establish the general applicability of the developed catalytic reaction, we screened various substrates with distinct functionalities. There was no drastic change in the yield of the hydrophosphination pro-

Fig. 5 Superimposition of the experimental absorption spectra on the TD-DFT computed spectra of [G.S/2 + E.S/2] species.
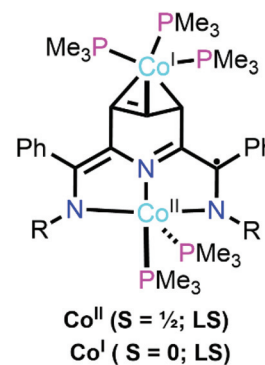
Scheme 3 The proposed electronic structure of **2** based on various experimental and theoretical investigations.
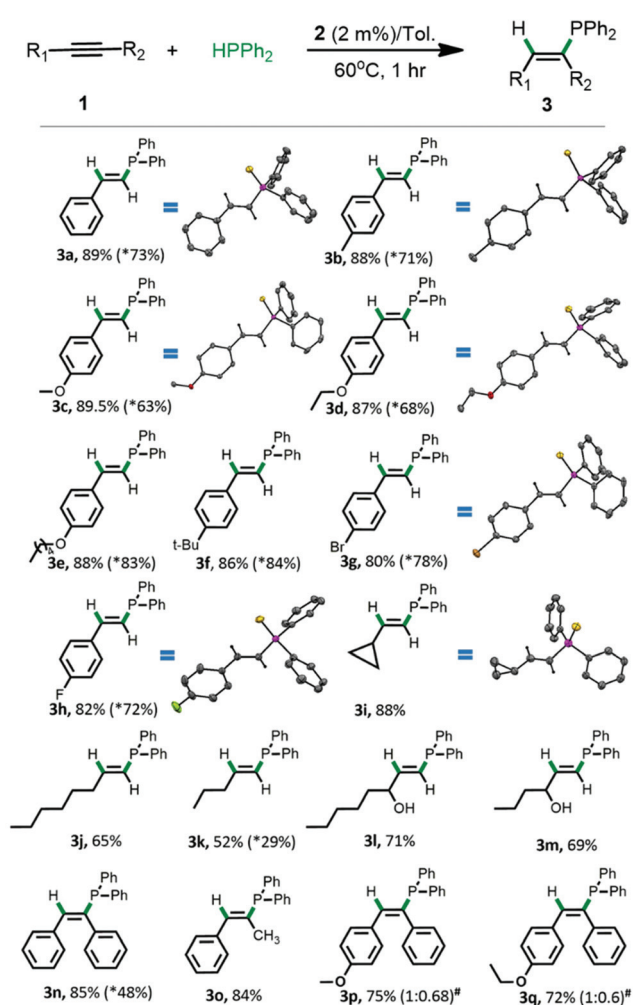
Scheme 4 Scope of the substrates.[a,b] [a] Condition: alkyne (0.575 mmol), HPPh$_2$(0.575 mmol), catalyst (**2**; 2.0 mol%), toluene (2 ml), 1 h @ 60 °C under argon atmosphere. [b] Isolated yield after sulfidation. * denotes the isolated yield of the product obtained with **1**, which is recalled again for comparison purposes.[37] # denotes the ratio of anti-Markovnikov and Markovnikov products obtained.

ducts when an electron-donating (**3b–3f**) or electron-withdrawing (**3g** and **3h**) group was present in the *para*-position of the aryl group compared with phenylacetylene.

In contrast to the certain nickel or palladium-catalyzed hydrophosphination reactions (where P–H addition happens only for aryl alkynes), **2** promotes the hydrophosphination reaction of electron-rich aliphatic alkynes (**3j** and **3k**). The reaction was successful even for a strained alkyne such as cyclopropyl alkyne, yielding a corresponding *E*-selective vinyl phosphine (**3i**) product without opening of the three-membered ring, which is further corroborated by the single-crystal X-ray structure. To the best of our knowledge, alkyne functionalized at the propargylic position, such as propargyl alcohol, amine, *etc.*, has not been explored for the hydrophosphination of alkynes, and only a handful of reports are known in this regard.[67,68] The α-hydroxy functionalized racemic 1-octyn-3-ol

and 1-hexyn-3-ol underwent hydrophosphination with anti-Markovnikov selectivity with a good yield (**3l** and **3m**; isolated yield after sulfidation ~70%). This discloses the versatility and robustness of the catalyst employed compared with the monometallic catalyst. We did not notice the formation of a *Z*-selective product under the reaction conditions followed by us, unlike the uncatalyzed hydrophosphination of propargylic alcohols/amines reported by Busacca and co-workers.[68] On the other hand, a ruthenium-catalyzed hydrophosphination reaction of propargylic alcohols was found to provide a *Z*-selective product predominantly due to the formation of a Ru-vinylidene intermediate.[67] The reverse stereoselectivity observed while employing **2** as a catalyst compared with the ruthenium catalyst reported by Dixneuf and co-workers implies that a distinct mechanism of the reaction was observed with the presented cobalt system.

On the other hand, a ruthenium-catalyzed hydrophosphination reaction of propargylic alcohols was found to provide a *Z*-selective product predominantly due to the formation of the Ru-vinylidene intermediate.[67] The reverse stereoselectivity observed when employing **2** as a catalyst compared with the ruthenium catalyst reported by Dixneuf and co-workers implies that a distinct mechanism of the reaction was observed with the presented cobalt system. Chiral phosphines are extensively used in asymmetric catalysis (both metal based and organocatalyzed); therefore, the success of this catalyst towards the catalytic reaction with α-functionalized racemic substrates will certainly pave the way to realizing a new generation of chiral phosphines *via* simple routes, which could potentially open a new avenue in asymmetric catalysis.

Despite several catalysts being effective against the terminal alkynes for the hydrophosphination reaction, their corresponding extension to the internal alkynes often failed to provide vinyl phosphine or did not provide any control over regioselectivity (with unsymmetrical alkynes) and stereoselectivity.[69] In contrast, **2** is effective in promoting the hydrophosphination not only of terminal alkynes, but also of the internal alkynes (**3n** and **3o**). We have noticed that the phosphine group adds to the carbon centre with a less sterically hindered side of the unsymmetrically substituted alkyne substrate (**3o**), while regioselectivity is lost when employing unsymmetrical alkynes such as **3p** and **3q**, *i.e.* both Markovnikov and anti-Markovnikov products were obtained. This is due to the absence of significant electronic bias at the two C centers of these substrates. Therefore, **2** is a rare example that has been found to promote the hydrophosphination reaction of internal alkynes whose catalytic activity is akin to the low-valence Co^0 catalyst ([Co(PMe$_3$)$_4$]; **1**) reported by us earlier.[37] Notably, the catalytic efficiency of **2** appears to be appreciably increased, particularly for the internal alkynes, where the yields of **3n** and **3o** were increased drastically compared with the catalytic activity of **1**. Besides, **1** failed to catalyze the hydrophosphination reaction of propargylic alcohol or amines and other α-functionalized racemic alkyne substrates under similar catalytic reaction conditions. This divergence

and robust catalytic activity of **2** (compared to **1**) could presumably be due to the unique coordination platform laid by the reduced pincer ligand and distinct electronic structure, and/or the cooperative effect offered by the mixed-valence oxidation state of the cobalt ions (*vide infra*).

To understand whether both the cobalt ions or either one of the cobalt ions in **2** is involved in the catalytic reaction, we performed both ^{1}H and ^{31}P NMR in d8-THF solution at 10 °C (Fig. 6). Initially, a stoichiometric equivalent of PPh$_2$H was added to **2**. For this reaction mixture, we observe well-resolved ^{1}H NMR signals in both the aliphatic region (0.5 to 3.0 ppm) and the aromatic region (6.5 to 8.5 ppm). In addition, a weak quartet of doublet ^{1}H NMR signal was observed at −16.35 ppm, which is attributed to cobalt hydride formation. This peak position for the Co–H in the negative region is consistent with the other M–H reported in the literature.[70,71] To rationalize the quartet of the doublet of this hydride signal, we further analyzed the ^{31}P NMR of this reaction mixture. At 10 °C, the bare complex **2** shows only three ^{31}P NMR signals at 33.2, 8.0 and −16 ppm. As assigned earlier, the ^{31}P signal at 33.2 ppm is attributed to the PMe$_3$ ligands bound to the Co^{II} ion, while the remaining peaks were assigned as the partially resolved ^{31}P signal of the PMe$_3$ group bound to the Co^{I}. Upon reacting PPh$_2$H with **2**, certain changes were noticed in the

spectral features. There is a peak in the ^{31}P NMR spectrum (34.0 ppm) that is slightly downfield shifted compared with its signal (33.2 ppm) observed in pure complex **2**. This suggests that the –PMe$_3$ group bound to Co^{II} in **2** is unaltered, *i.e.* not involved in the catalytic process. Further, there is no signature for the presence of the free PMe$_3$ group in the reaction mixture upon treating PPh$_2$H with **2** (usually a ^{31}P NMR signal observed around −62.5 ppm for free PMe$_3$), indicating that an oxidative addition is happening at the Co^{I} centre.

However, to overcome the steric crowd around the Co^{I} upon oxidative addition, the η^3-allylic-like coordination environment around this metal centre presumably changes to a η^1-coordination environment with an octahedral geometry around Co^{III} with three –PMe$_3$ ligands, one hydride ligand and one PPh$_2$ ligand. Consequently, the –PPh$_2$ group bound to this Co^{III} ion shows a ^{31}P signal at 42.5 ppm. The chemical shift value observed for the metal-bound –PPh$_2$ group is consistent with the other literature report.[37]

In such a situation, the fluxional behaviour that was observed earlier for the pure complex **2** was arrested and therefore three additional ^{31}P signals were observed, spanning 10 to −25 ppm. This coordination environment around Co^{III} ion also rationalizes the quartet of the doublet ^{1}H NMR signal observed for the hydride ion. The structural flexibility offered by the pincer ligand (L$_1$) is observed to be the key for the exceptional catalytic activity of **2** compared with the mononuclear metal catalyst. Further, coordination of the alkyne
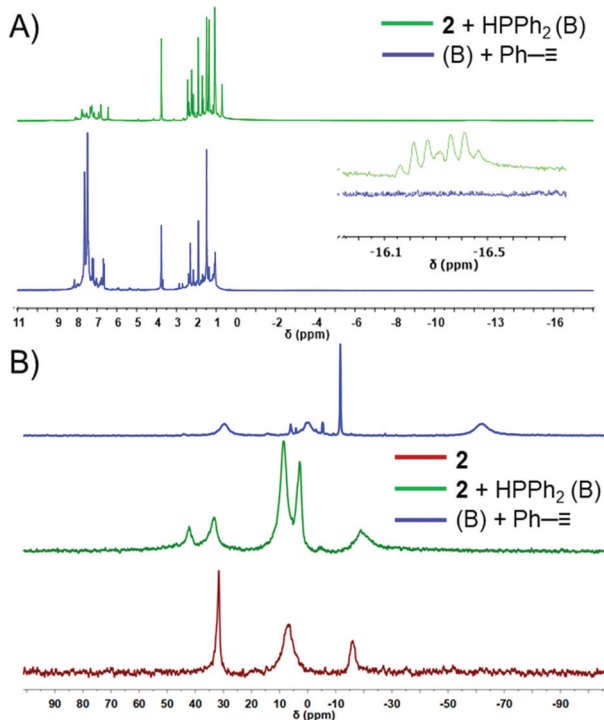

Fig. 6 The change in ^{1}H-NMR (panel A) and ^{31}P NMR (panel B) spectral features observed in the intermediate generated upon treating **2** with the stoichiometric equivalent of HPPh$_2$ (green trace) and the intermediate along with phenylacetylene substrate (blue trace red trace). ^{31}P-NMR spectrum of **2** (brown-red) provided in panel B for comparison purposes. The NMR spectra were recorded in d8-THF using 400 MHz instrument at −10 °C.
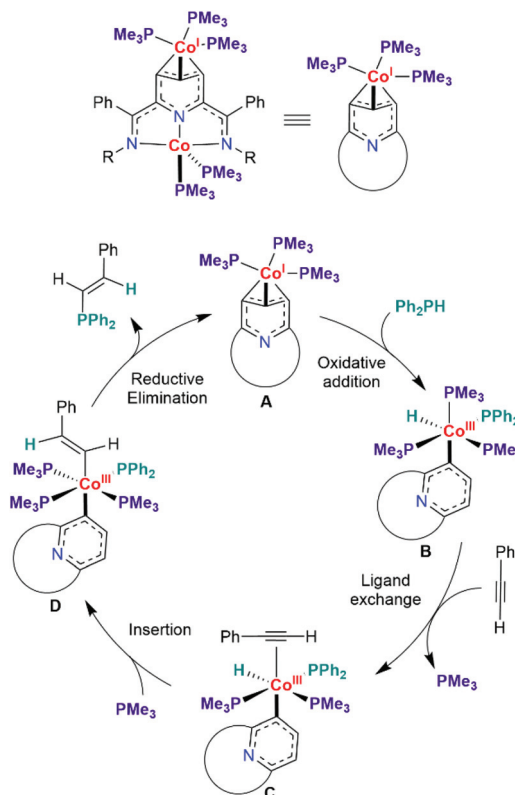
Scheme 5 Proposed mechanism for the catalytic cycle.

with intermediate **B** *via* ligand replacement leads to **C** that subsequently inserts between cobalt and carbon, leading to intermediate **D**. The following changes were noticed in the ^{31}P NMR spectrum recorded at room temperature: (1) vinyl phosphine product formation was observed at −11.6 ppm with the concomitant disappearance of the peak observed at 42.5 ppm; (2) the presence of the free PMe$_3$ group in the reaction mixture was observed at −62.5 ppm, which evidently exemplifies that the PMe$_3$ ligand bound to Co^{III} ion is being released to accommodate the incoming alkyne substrate in the vicinity of the metal coordination site; and (3) two additional ^{31}P NMR signals at 30 and −1.0 ppm, respectively, are attributed to the two PMe$_3$ groups bound to the silent spectator Co^{II} metal ion and a PMe$_3$ group bound to the cobalt ion upon reductive elimination of the product, thus regenerating the active Co^{I}(allylic-like) catalyst. Thus, the unique platform laid by the NNN pincer ligand is responsible for the excellent catalytic activity of **2**, including propargylic substrates. This experimental observation is consistent with the theoretical prediction that Co^{I} is expected to actively take part in the catalytic reaction compared with Co^{II} as the HOMO–LUMO gap for the former (1.6 eV) is much smaller than that for the latter (2.5 eV). Based on detailed NMR spectroscopic studies, we propose the reaction mechanism shown in Scheme 5.

Conclusions

In summary, the X-ray and the electronic structure of the mixed-valence dinuclear cobalt $[(PMe_3)_2Co^{II}(L_1{}^{3-})Co^I(PMe_3)_3]$ (**2**) were determined unambiguously. The X-band EPR experiments performed at 77 K and room temperature disclose that **2** possesses a singlet as a ground state. This is consistent with the electronic structure of **2** determined from DFT calculations where $S = 0$ as the overall ground state arises due to the antiferromagnetic coupling between low-spin Co^{II} and the resultant $S = 1/2$ arising from the three-electron-reduced L$_1$ in **2**. The general hydrophosphination reaction developed using **2** can be applied to the alkyl/aryl/cyclic terminal alkynes, symmetric/unsymmetric internal alkynes, and α-functionalized alkynes (such as –OH). This straightforward catalytic reaction does not require any additives like Cs$_2$CO$_3$, *n*-BuLi *etc*. In all the cases, the supra facial syn addition of P–H across the C–C triple bond results in regio- and stereoselective *E*-vinylphosphines. The control experiments performed using **1** as a catalyst disclose that the binuclear cobalt complex **2** acts as an efficient catalyst, which is attributed to the distinct electronic structure and coordination modes offered by the ligand in **2**. Besides, based on the detailed NMR investigation, we have not only shed light on the certain intermediates involved in the catalytic cycle but also unveiled the participation of the redox-active ligand in the catalytic cycle. Further, we have identified the Co^{I} ion as exclusively and actively participating in the reaction mechanism, which is in line with the theoretical prediction, and the Co^{II} in **2** is presumed to be a silent spectator.

Conflicts of interest

The author declares no conflict of interest.

Acknowledgements

References

1 Y. Bai, W. Chen, J. Li and C. Cui, Chemistry of s-, p- and f-block metal complexes with ene-diamido ligands, *Coord. Chem. Rev.*, 2019, **383**, 132–154.

2 O. R. Luca and R. H. Crabtree, Redox-active ligands in catalysis, *Chem. Soc. Rev.*, 2013, **42**, 1440–1459.

3 V. Lyaskovskyy and B. de Bruin, Redox non-innocent ligands: Versatile new tools to control catalytic reactions, *ACS Catal.*, 2012, **2**, 270–279.

4 Z. Flisak and W.-H. Sun, Progression of diiminopyridines: from single application to catalytic versatility, *ACS Catal.*, 2015, **5**, 4713–4724.

5 V. K. K. Praneeth, M. R. Ringenberg and T. R. Ward, Redox-active ligands in catalysis, *Angew. Chem., Int. Ed.*, 2012, **51**, 10228–10234.

6 H. Agarwala, F. Ehret, A. D. Chowdhury, S. Maji, S. M. Mobin, W. Kaim and G. K. Lahiri, Electronic structure and catalytic aspects of $[Ru(tpm)(bqdi)(Cl/H_2O)]_n$, tpm=tris(1-pyrazolyl)methane and bqdi=o-benzoquinonediimine, *Dalton Trans.*, 2013, **42**, 3721–3734.

7 W. Kaim, The transition metal coordination chemistry of anion radicals, *Coord. Chem. Rev.*, 1987, **76**, 187–235.

8 A. Arnold, R. J. Dougherty, C. R. Carr, L. C. Reynolds, J. C. Fettinger, A. Augustin and L. A. Berben, A stable organo-aluminum analyte enables multielectron storage for a nonaqueous redox flow battery, *J. Phys. Chem. Lett.*, 2020, **11**, 8202–8207.

9 D. P. Cladis, J. J. Kiernicki, P. E. Fanwick and S. C. Bart, Multi-electron reduction facilitated by a trianionic pyridine (diimine) ligand, *Chem. Commun.*, 2013, **49**, 4169–4171.

10 D. Enright, S. Gambarotta, G. P. A. Yap and P. H. M. Budzelaar, The ability of the α,α'-diiminopyridine ligand system to accept negative charge: Isolation of paramagnetic and diamagnetic trianions, *Angew. Chem., Int. Ed.*, 2002, **41**, 3873–3876.

11 A. M. Tondreau, S. C. E. Stieber, C. Milsmann, E. Lobkovsky, T. Weyhermuller, S. P. Semproni and P. J. Chirik, Oxidation and reduction of bis(imino)pyridine

iron dinitrogen complexes: Evidence for formation of a chelate trianion, *Inorg. Chem.*, 2013, **52**, 635–646.

12 S. C. Bart, K. Chłopek, E. Bill, M. W. Bouwkamp, E. Lobkovsky, F. Neese, K. Wieghardt and P. J. Chirik, Electronic structure of bis(imino)pyridine iron dichloride, monochloride, and neutral ligand complexes: A combined structural, spectroscopic, and computational study, *J. Am. Chem. Soc.*, 2006, **128**, 13901–13912.

13 A. C. Bowman, C. Milsmann, E. Bill, Z. R. Turner, E. Lobkovsky, S. DeBeer, K. Wieghardt and P. J. Chirik, Synthesis and electronic structure determination of N-alkyl-substituted bis(imino)pyridine iron imides exhibiting spin crossover behavior, *J. Am. Chem. Soc.*, 2011, **133**, 17353–17369.

14 N. H. Anderson, S. O. Odoh, Y. Yao, U. J. Williams, B. A. Schaefer, J. J. Kiernicki, A. J. Lewis, M. D. Goshert, P. E. Fanwick, E. J. Schelter, J. R. Walensky, L. Gagliardi and S. C. Bart, Harnessing redox activity for the formation of uranium tris(imido) compounds, *Nat. Chem.*, 2014, **6**, 919–926.

15 J. Scott, I. Vidyaratne, I. Korobkov, S. Gambarotta and P. H. M. Budzelaar, Multiple pathways for dinitrogen activation during the reduction of an Fe bis(iminepyridine) complex, *Inorg. Chem.*, 2008, **47**, 896–911.

16 N. Rahimi, B. de Bruin and P. H. M. Budzelaar, Balance between metal and ligand reduction in diiminepyridine complexes of Ti, *Organometallics*, 2017, **36**, 3189–3198.

17 B. A. Jazdzewski and W. B. Tolman, Understanding the copper-phenoxyl radical array in galactose oxidase: Contributions from synthetic modeling studies, *Coord. Chem. Rev.*, 2000, **200–202**, 633–685.

18 P. Chaudhuri and K. Wieghardt, Phenoxyl radical complexes, *Prog. Inorg. Chem.*, 2001, **50**, 151–216.

19 E. A. Lewis and W. B. Tolman, Reactivity of dioxygen-copper systems, *Chem. Rev.*, 2004, **104**, 1047–1076.

20 R. A. Zarkesh, J. W. Ziller and A. F. Heyduk, Four-electron oxidative formation of aryl diazenes using a tantalum redox-active ligand complex, *Angew. Chem., Int. Ed.*, 2008, **47**, 4715–4718.

21 W. Kaim and B. Schwederski, Non-innocent ligands in bioinorganic chemistry: An overview, *Coord. Chem. Rev.*, 2010, **254**, 1580–1588.

22 J. Rittle and M. T. Green, Cytochrome P450 compound I: Capture, characterization, and C–H bond activation kinetics, *Science*, 2010, **330**, 933–937.

23 A. F. Heyduk, R. A. Zarkesh and A. I. Nguyen, Designing catalysts for nitrene transfer using early transition metals and redox-active ligands, *Inorg. Chem.*, 2011, **50**, 9849–9863.

24 E. R. King, E. T. Hennessy and T. A. Betley, Catalytic C–H bond amination from high-spin iron imido complexes, *J. Am. Chem. Soc.*, 2011, **133**, 4917–4923.

25 A. I. Nguyen, R. A. Zarkesh, D. C. Lacy, M. K. Thorson and A. F. Heyduk, Catalytic nitrene transfer by a zirconium(IV) redox-active ligand complex, *Chem. Sci.*, 2011, **2**, 166–169.

26 L. Ackermann, Air- and moisture-stable secondary phosphine oxides as preligands in catalysis, *Synthesis*, 2006, 1557–1571, DOI: **10.1055/s-2006-926427**.

27 E. Rafter, T. Gutmann, F. Loew, G. Buntkowsky, K. Philippot, B. Chaudret and P. W. N. M. van Leeuwen, Secondary phosphine oxides as pre-ligands for nano-particle stabilization, *Catal. Sci. Technol.*, 2013, **3**, 595–599.

28 V. Koshti, S. Gaikwad and S. H. Chikkali, Contemporary avenues in catalytic PH bond addition reaction: A case study of hydrophosphination, *Coord. Chem. Rev.*, 2014, **265**, 52–73.

29 D. S. Glueck, Metal-catalyzed asymmetric synthesis of P-stereogenic phosphines, *Synlett*, 2007, 2627–2634, DOI: **10.1055/s-2007-991077**.

30 P. G. Pringle and M. B. Smith, Platinum(0)-catalyzed hydrophosphination of acrylonitrile, *J. Chem. Soc., Chem. Commun.*, 1990, 1701–1702, DOI: **10.1039/c39900001701**.

31 J. A. Gladysz, R. B. Bedford, M. Fujita, F. P. Gabbai, K. I. Goldberg, P. L. Holland, J. L. Kiplinger, M. J. Krische, J. Louie, C. C. Lu, J. R. Norton, M. A. Petrukhina, T. Ren, S. S. Stahl, T. D. Tilley, C. E. Webster, M. C. White and G. T. Whiteker, Organometallics roundtable 2013–2014, *Organometallics*, 2014, **33**, 1505–1527.

32 S.-I. Kawaguchi, S. Nagata, A. Nomoto, M. Sonoda and A. Ogawa, A highly regioselective palladium-catalyzed hydrophosphination of alkynes using a diphosphine–hydrosilane binary system, *J. Org. Chem.*, 2008, **73**, 7928–7933.

33 S. Nagata, S.-I. Kawaguchi, M. Matsumoto, I. Kamiya, A. Nomoto, M. Sonoda and A. Ogawa, A highly regioselective hydrophosphination of terminal alkynes with tetraphenyldiphosphine in the presence of palladium catalyst, *Tetrahedron Lett.*, 2007, **48**, 6637–6640.

34 L. Rosenberg, Mechanisms of metal-catalyzed hydrophosphination of alkenes and alkynes, *ACS Catal.*, 2013, **3**, 2845–2855.

35 M. A. Kazankova, M. O. Shulyupin and I. P. Beletskaya, Catalytic hydrophosphination of alkenyl alkyl ethers, *Synlett*, 2003, 2155–2158, DOI: **10.1055/s-2003-42092**.

36 M. O. Shulyupin, M. A. Kazankova and I. P. Beletskaya, Catalytic hydrophosphination of styrenes, *Org. Lett.*, 2002, **4**, 761–763.

37 J. Rajpurohit, P. Kumar, P. Shukla, M. Shanmugam and M. Shanmugam, Mechanistic investigation of well-defined cobalt catalyzed formal E-selective hydrophosphination of alkynes, *Organometallics*, 2018, **37**, 2297–2304.

38 H. Wang, Y. Li, Z. Tang, S. Wang, H. Zhang, H. Cong and A. Lei, Z-Selective addition of diaryl phosphine oxides to alkynes via photoredox catalysis, *ACS Catal.*, 2018, **8**, 10599–10605.

39 M. M. I. Basiouny, D. A. Dollard and J. A. R. Schmidt, Regioselective single and double hydrophosphination and hydrophosphinylation of unactivated alkynes, *ACS Catal.*, 2019, **9**, 7143–7153.

40 V. A. Pollard, A. Young, R. McLellan, A. R. Kennedy, T. Tuttle and R. E. Mulvey, Lithium-aluminate-catalyzed

hydrophosphination applications, *Angew. Chem., Int. Ed.*, 2019, **58**, 12291–12296.

41 X.-T. Liu, X.-Y. Han, Y. Wu, Y.-Y. Sun, L. Gao, Z. Huang and Q.-W. Zhang, Ni-catalyzed asymmetric hydrophosphination of unactivated alkynes, *J. Am. Chem. Soc.*, 2021, **143**, 11309–11316.

42 H. Hu and C. Cui, Synthesis of calcium and ytterbium complexes supported by a tridentate imino-amidinate ligand and their application in the intermolecular hydrophosphination of alkenes and alkynes, *Organometallics*, 2012, **31**, 1208–1211.

43 M. Frisch, G. Trucks, H. Schlegel, G. Scuseria, M. Robb, J. Cheeseman, G. Scalmani, V. Barone, B. Mennucci and G. Petersson, *Gaussian 09*, Gaussian, Inc., Wallingford, CT, 2009, **32**, 5648–5652.

44 M. Frisch, G. Trucks, H. Schlegel, G. Scuseria, M. Robb, J. Cheeseman, G. Scalmani, V. Barone, B. Mennucci and G. Petersson, *Gaussian 09, rev. D. 01*, Gaussian Inc., Wallingford CT, 2009.

45 L. Noodleman, D. A. Case and A. Aizman, Broken symmetry analysis of spin coupling in iron–sulfur clusters, *J. Am. Chem. Soc.*, 1988, **110**, 1001–1005.

46 A. D. Becke, Density-functional exchange-energy approximation with correct asymptotic behavior, *Phys. Rev. A*, 1988, **38**, 3098.

47 A. D. Becke, Density–functional thermochemistry. I. The effect of the exchange-only gradient correction, *J. Chem. Phys.*, 1992, **96**, 2155–2160.

48 A. Schäfer, C. Huber and R. Ahlrichs, Fully optimized contracted Gaussian basis sets of triple zeta valence quality for atoms Li to Kr, *J. Chem. Phys.*, 1994, **100**, 5829–5835.

49 R. Bauernschmitt, M. Häser, O. Treutler and R. Ahlrichs, Calculation of excitation energies within time-dependent density functional theory using auxiliary basis set expansions, *Chem. Phys. Lett.*, 1997, **264**, 573–578.

50 F. Weigend and R. Ahlrichs, Balanced basis sets of split valence, triple zeta valence and quadruple zeta valence quality for H to Rn: Design and assessment of accuracy, *Phys. Chem. Chem. Phys.*, 2005, **7**, 3297–3305.

51 B. Civalleri, C. M. Zicovich-Wilson, L. Valenzano and P. Ugliengo, B3LYP augmented with an empirical dispersion term (B3LYP-D*) as applied to molecular crystals, *CrystEngComm*, 2008, **10**, 405–410.

52 F. Weinhold, Natural bond orbital analysis: a critical overview of relationships to alternative bonding perspectives, *J. Comput. Chem.*, 2012, **33**, 2363–2379.

53 G. Zhurko and D. Zhurko, *ChemCraft, version 1.6*, 2009, URL: http://www.chemcraftprog.com.

54 Y. G. Borod'ko, S. I. Vetchinkin, S. L. Zimont, I. N. Ivleva and Y. M. Shul'ga, Nature of satellites in x-ray photoelectron spectra XPS of paramagnetic cobalt(ɪɪ) compounds, *Chem. Phys. Lett.*, 1976, **42**, 264–267.

55 J. S. H. Q. Perera, D. C. Frost and C. A. McDowell, X-ray photoelectron spectroscopy of cobalt(ɪɪ), nickel(ɪɪ), and copper(ɪɪ) acetylacetonate vapors, *J. Chem. Phys.*, 1980, **72**, 5151–5158.

56 J. E. Huheey, The electronegativity of multiply bonded groups, *J. Phys. Chem.*, 1966, **70**, 2086–2092.

57 H. Xu, J. Li, Z. Wu, J. Zou, Z. Xu, X. You and Z. Dong, Synthesis and x-ray crystal structure of a mixed-valent cobalt complex, $Co_2Cl_5(py)_5$, *Polyhedron*, 1993, **12**, 2261–2264.

58 J. Rajpurohit and M. Shanmugam, The molecular and electronic structure of an unusual cobalt NNO pincer ligand complex, *Dalton Trans.*, 2019, **48**, 7378–7387.

59 J. Scott, S. Gambarotta, I. Korobkov, Q. Knijnenburg, B. De Bruin and P. H. M. Budzelaar, Formation of a paramagnetic Al complex and extrusion of Fe during the reaction of (diiminepyridine)Fe with AlR_3 (R=Me, Et), *J. Am. Chem. Soc.*, 2005, **127**, 17204–17206.

60 R. A. Lewis, K. C. MacLeod, B. Q. Mercado and P. L. Holland, Geometric and redox flexibility of pyridine as a redox-active ligand that can reversibly accept one or two electrons, *Chem. Commun.*, 2014, **50**, 11114–11117.

61 X. Zhou, Y. Xu and G. Dong, Deacylation-aided C–H alkylative annulation through C–C cleavage of unstrained ketones, *Nat. Catal.*, 2021, **4**, 703–710.

62 A. Di Giuseppe, R. De Luca, R. Castarlenas, J. J. Perez-Torrente, M. Crucianelli and L. A. Oro, Double hydrophosphination of alkynes promoted by rhodium: The key role of an N-heterocyclic carbene ligand, *Chem. Commun.*, 2016, **52**, 5554–5557.

63 J. Yuan, L. Zhu, J. Zhang, J. Li and C. Cui, Sequential addition of phosphine to alkynes for the selective synthesis of 1,2-diphosphinoethanes under catalysis. Well-defined NHC-copper phosphides vs. in situ $CuCl_2$/NHC catalyst, *Organometallics*, 2017, **36**, 455–459.

64 Q. Liu, C. Wang, X. Zhang, M. Xue, Y. Yao, Y. Zhang and Q. Shen, Synthesis and molecular structures of divalent bridged bis(guanidinate) europium complexes and their application in intermolecular hydrophosphination of alkenes and alkynes, *New J. Chem.*, 2016, **40**, 10447–10454.

65 M. Hayashi, Y. Matsuura and Y. Watanabe, Regio- and stereoselective synthesis of alkenylphosphines: A rhodium-catalyzed hydrophosphination of alkynes using a silylphosphine, *J. Org. Chem.*, 2006, **71**, 9248–9251.

66 B. J. Ackley, J. K. Pagano and R. Waterman, Visible-light and thermal driven double hydrophosphination of terminal alkynes using a commercially available iron compound, *Chem. Commun.*, 2018, **54**, 2774–2776.

67 F. Jerome, F. Monnier, H. Lawicka, S. Derien and P. H. Dixneuf, Ruthenium catalyzed regioselective hydrophosphination of propargyl alcohols, *Chem. Commun.*, 2003, 696–697, DOI: 10.1039/b212408d.

68 C. A. Busacca, B. Qu, E. Farber, N. Haddad, N. Gret, A. K. Saha, M. C. Eriksson, J.-P. Wu, K. R. Fandrick, S. Han, N. Grinberg, S. Ma, H. Lee, Z. Li, M. Spinelli, A. Gold, G. Wang, P. Wipf and C. H. Senanayake, Hydrophosphination of propargylic alcohols and amines with phosphine boranes, *Org. Lett.*, 2013, **15**, 1132–1135.

69 Y. Moglie, M. J. Gonzalez-Soria, I. Martin-Garcia, G. Radivoy and F. Alonso, Catalyst- and solvent-free hydrophosphination and multicomponent hydrothiophosphina-

tion of alkenes and alkynes, *Green Chem.*, 2016, **18**, 4896–4907.

70 J. J. Levison and S. D. Robinson, Hydrido(triaryl phosphite) complexes of cobalt, rhodium, and iridium, *Chem. Commun.*, 1968, 1405–1406, DOI: **10.1039/C19680001405**.

71 L. S. Merz, C. K. Blasius, H. Wadepohl and L. H. Gade, Square planar cobalt(ɪɪ) hydride versus T-shaped cobalt(ɪ): Structural characterization and dihydrogen activation with PNP–cobalt pincer complexes, *Inorg. Chem.*, 2019, **58**, 6102–6113.